Int J CARS (2013) 8:193–205
DOI 10.1007/s11548-012-0767-5

ORIGINAL ARTICLE

Fast lung nodule detection in chest CT images using cylindrical nodule-enhancement filter

Atsushi Teramoto · Hiroshi Fujita

Received: 4 February 2012 / Accepted: 24 May 2012 / Published online: 9 June 2012

Abstract
Purpose Existing computer-aided detection schemes for lung nodule detection require a large number of calculations and tens of minutes per case; there is a large gap between image acquisition time and nodule detection time. In this study, we propose a fast detection scheme of lung nodule in chest CT images using cylindrical nodule-enhancement filter with the aim of improving the workflow for diagnosis in CT examinations.
Methods Proposed detection scheme involves segmentation of the lung region, preprocessing, nodule enhancement, further segmentation, and false-positive (FP) reduction. As a nodule enhancement, our method employs a cylindrical shape filter to reduce the number of calculations. False positives (FPs) in nodule candidates are reduced using support vector machine and seven types of characteristic parameters.
Results The detection performance and speed were evaluated experimentally using Lung Image Database Consortium publicly available image database. A 5-fold cross-validation result demonstrates that our method correctly detects 80 % of nodules with 4.2 FPs per case, and detection speed of proposed method is also 4–36 times faster than existing methods.
Conclusion Detection performance and speed indicate that our method may be useful for fast detection of lung nodules in CT images.

A. Teramoto (✉)
Faculty of Radiological Technology, School of Health Sciences, Fujita Health University, 1-98 Dengakugakubo, Kutsukake-cho, Toyoake-city, Aichi 470-1192, Japan
e-mail: teramoto@fujita-hu.ac.jp

H. Fujita
Department of Intelligent Image Information, Graduate School of Medicine Gifu University, 1-1 Yanagido, Gifu-city, Gifu 501-1194, Japan

Keywords Computer-aided detection (CAD) · Lung · Nodule · Computed tomography (CT) · Image processing · Fast detection

Abbreviations

CAD	Computer-aided detection
CNEF	Cylindrical nodule-enhancement filter
C-SVC	C-support vector classification
CT	Computed tomography
FROC	Free-response receiver operating characteristic
GGO	Ground glass opacity
LIDC	Lung image database consortium
MIP	Maximum intensity projection
PET	Positron emission tomography
SVM	Support vector machine

Introduction

Lung cancer is a serious public health problem in the United States, Europe, and many other countries, as it is a leading cause of death, in terms of cancer, for men and women. Detection and treatment at an early stage are required to effectively overcome this burden. X-ray computed tomography (CT) has recently been adopted as a mass-screening tool for lung cancer diagnosis [1], enabling a rapid improvement in the ability to detect tumors early. According to the results from the National Lung Screening Trial [2], screening with low-dose CT scans cuts lung cancer deaths by 20 %. A greater number of CT examinations are expected to be adopted for lung screening in the future; however, CT scans generate a large number of images that must be read by the radiologist, and avoiding diagnostic reading errors is a pressing challenge.

Computer-aided detection (CAD) provides computer output as a "second opinion" to assist radiologists in diagnosing

various diseases from medical images. Many CAD methods for lung nodule detection have been developed [3–12].

Yamamoto et al. [3] proposed an enhancement filter, the Quoit Filter, that has large ring and disk filters. The filter enhances the nodule by calculating the difference in the output of the ring and disk filter. They also proposed a three-dimensional (3D) extension. Lee et al. [4] used a template matching technique to detect lung nodules in chest CT scans. A genetic algorithm was designed to determine the target position and to select a template image from the reference patterns. The four reference templates were established according to the gray-level values of 3D Gaussian distributions. Li et al. [7] proposed three selective enhancement filters for dots, lines, and planes, which can simultaneously enhance objects of a specific shape and suppress other objects. They blurred the CT image with a Gaussian kernel that matched the size of the nodule to be detected before calculating the eigenvalues of the Hessian matrix that were used for selective enhancement. They used multiple scales of the Gaussian kernel to find a match with the nodule size.

Recent studies employ the publicly available testing database provided by the Lung Image Database Consortium (LIDC) to evaluate the detection performance of CAD schemes [13–20]. Way and Sahiner et al. [13,14] proposed a nodule detection scheme using a 3D active contour method. Opfer et al [15] proposed a CAD scheme based on distance transformations for various thresholds and subsequent crest line extraction. Golosio et al. [16] proposed the nodule detection method using multi-threshold surface triangulation approach. Messay et al. [17] employed a local contrast enhancement filter that followed the nodule enhancement method used for the chest radiographs [21]. Riccardi et al. [18] developed CAD scheme using 3D radial transform, scale space technique, and Zernike MIP classification. Camarlinghi et al. [19] proposed combined nodule detection using existing algorithms. Tan et al. [20] introduced nodule- and vessel-enhancement filter in a nodule detection step, feature selection, and classification methodology. These schemes have a sensitivity of 70–80 % with a false positive (FP) per case of less than 10. However, these methods require a large number of calculations and tens of minutes per case. On the other hand, current CT units have the capability of generating lung volume images within 30 s per scan. There is a large gap between image acquisition time and nodule detection time.

In this study, a fast CAD scheme for lung nodule detection is investigated with the aim of reducing the above gap, and improving the workflow for diagnosis in CT examinations.

In this paper, we propose a fast CAD scheme for lung nodule detection in CT images. We employed a cylindrical shape filter as a fast enhancement method for lung nodules in 3 dimensions. FPs in nodule candidates are reduced using support vector machine (SVM) together with seven characteristic shape parameters. In the experiments, the capability of our method is evaluated by using the LIDC database. Detection performance and detection speed of the proposed method are also compared to existing CAD schemes.

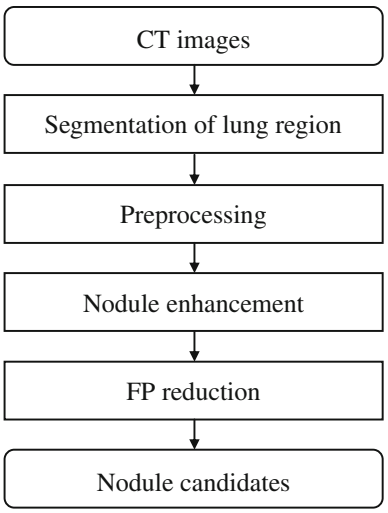

Fig. 1 Flow chart for the detection of lung nodules from CT images

Methods

Overview

The scheme developed for lung nodule detection includes several major steps: segmentation of the lung region, preprocessing, nodule enhancement, further segmentation, and FP reduction, as shown in Fig. 1. The segmentation of the lung region is determined using lung CT images. Preprocessing for the separation of the blood vessels and nodules is then performed followed by nodule enhancement using the cylindrical shape filter. Finally, we classify the nodules based on SVM using characteristic features.

Segmentation of lung region

In the first process of our CAD scheme, the lung region is segmented automatically from CT images in order to prevent FPs outside this region. We introduced three major conventional steps as follows: (1) extraction of an initial lung region by using thresholding based on the Hounsfield value (cut-off $= -400$) (2). Removal of invalid voxels outside the body (3). Filling the lack of blood vessels and lung nodules using the mathematical morphology operation. Figure 2 shows images of each step in the lung region segmentation.

Nodule enhancement using cylindrical nodule-enhancement filter

This is the essential technique for lung nodule detection. However, 3D enhancement requires a large number of

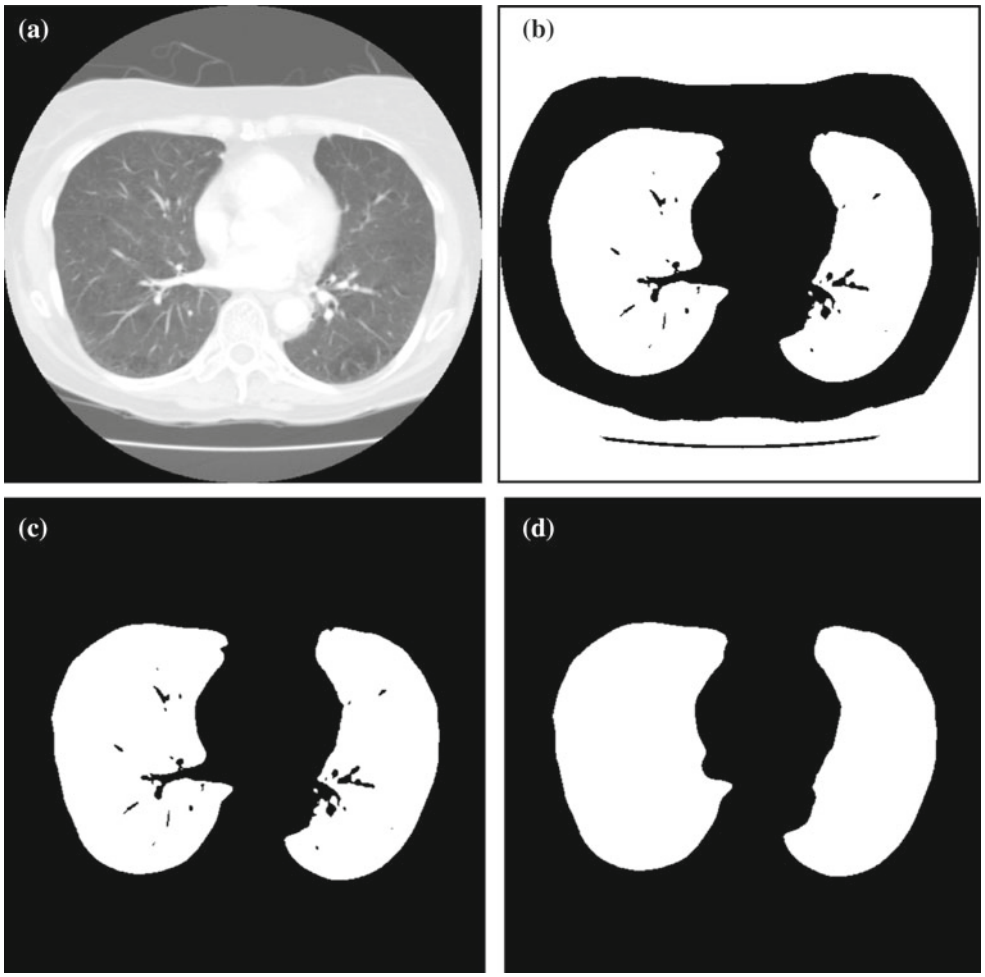

Fig. 2 Steps in the lung region segmentation. **a** Original image, **b** image after thresholding has been applied (cut-off = −400), **c** image after removal of pixels outside the lung, and **d** final output (*white pixels*) of the lung region segmentation after performing mathematical morphology filter

calculations, and the enhancement step makes up the greater part of the total calculations in the CAD scheme. In this paper, we propose a fast enhancement method named as a cylindrical nodule-enhancement filter (CNEF).

The CNEF has a cylindrical shape of radius r_1 and height $2r_1$ (Fig. 3).The output of the filter is calculated according to the following equations,

$$c(x, y, z) = f(x, y, z) - \max_{(x_c, y_c, z_c \in K_{\mathrm{CNEF}})} \left\{ f(x - x_c, y - y_c, z - z_c) \;\middle|\; \begin{array}{l} x_c^2 + y_c^2 \leq r_1^2 \;\text{ and } z_c = \pm r_1 \\ x_c^2 + y_c^2 = r_1^2 \;\text{ and } -r_1 < z_c < r_1 \end{array} \right\}, \quad (1)$$

where $f(x, y, z)$ is the input image, $c(x, y, z)$ is the output image, and K_{CNEF} is the filter kernel of the CNEF.

The CNEF represents the difference between the value of the centre voxel and the maximum value on the cylinder surface (sidewall, top, and bottom lids). When blood vessels penetrate the filter, the values of these two regions are identical, and the output of the filter decreases. In contrast, when there is an isolated nodule within the cylinder, only the centre

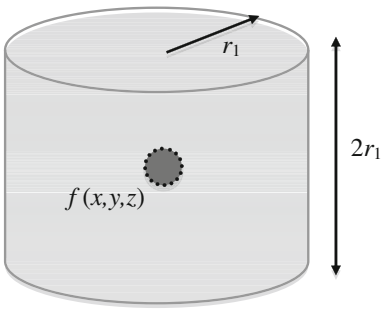

Fig. 3 Structure of the cylindrical filter. The filter outputs the difference between the value of the pixel at the centre of the cylinder around (x, y, z), $f(x, y, z)$ and the maximum pixel value on the cylinder surface

voxel has a high value, and the output of the filter increases. Thus, the CNEF enhances the nodule selectively based on the object shape.

The cylinder surface of CNEF can be divided into a sidewall and two lids (top and bottom). Here, the maximum value on the cylinder sidewall is equivalent to the maximum value on the circle whose radius is r_1 in a maximum intensity projection (MIP) image of slab width $2r_1$. This means that the 3D calculation for the cylinder sidewall is replaced by 2D processing using a MIP image. It is note that only one of MIP processing is required, while all voxels in one slice are processed. The outputs of two lids are equal to the output of morphological filter [22] that output the maximum value in a circle with radius r_1 at $z = \pm r_1$. After the maximum values of the cylinder sidewall and lids are calculated, the largest one is taken as the final output of the cylinder. In this manner, the CNEF uses only three 2D images, so significant reduction in the number of calculation is attained.

CNEF enhances nodules when nodule size is less than filter size. However, if filter size is much larger than nodule size, output of CNEF may decrease because filter kernel contact with lung structures such as bronchus, blood vessels, and lung wall. Therefore, filters of 2 sizes (diameter = 10–20 mm) were applied to each voxel; the highest filter output was automatically adopted as the final output.

In order to evaluate the performance of the filter, we designed a 3D digital phantom, which includes simulated spherical nodules with diameters of 6, 8, and 10 mm, and

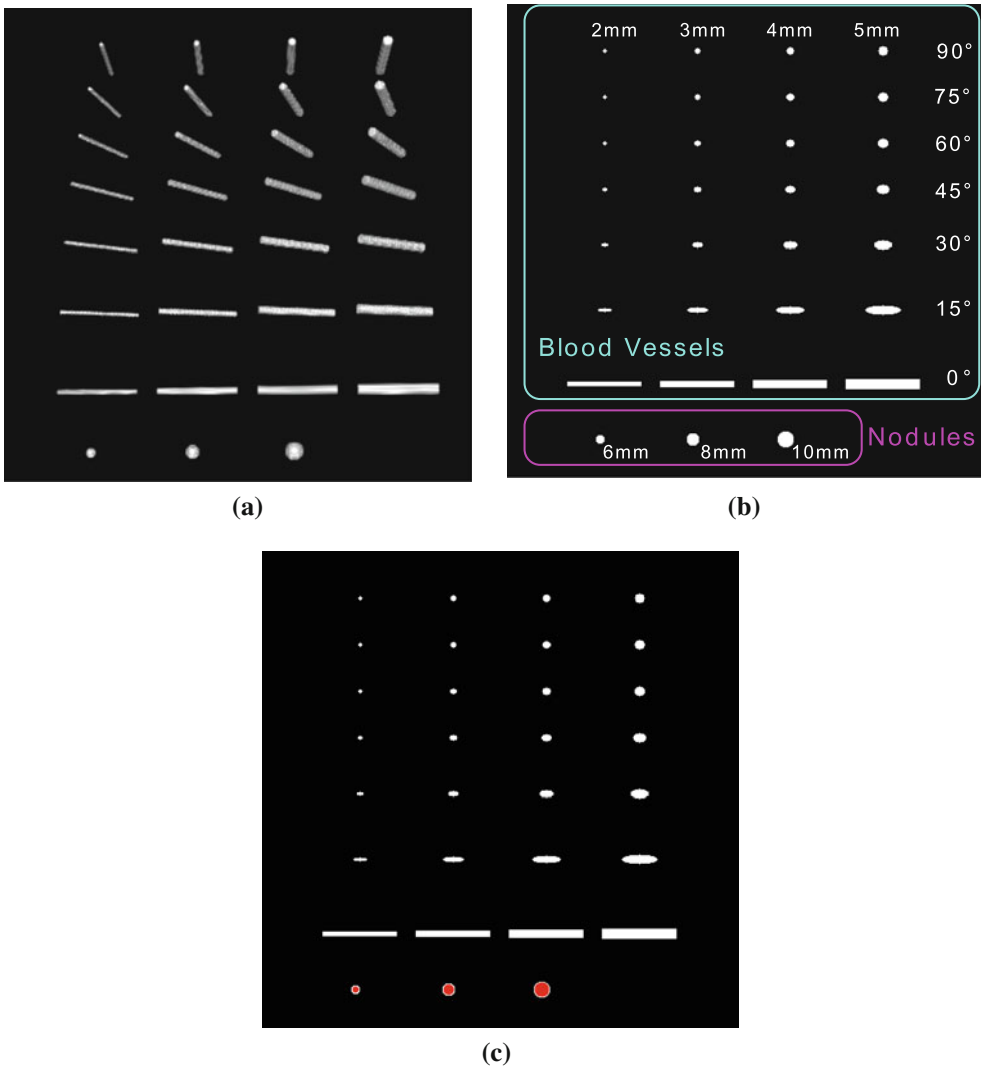

Fig. 4 Digital phantom and detection result. **a** Volume-rendered image of the phantom. **b** Slice images of the phantom. The digital phantom consists of spherical nodules (diameters of 6, 8, and 10 mm) and blood vessels (diameters of 2, 3, 4, and 5 mm). The blood vessels are positioned at angles between 0 and 90° in relation to the *X*–*Y* slice image. **c** Detection result of the nodule. Red regions indicate positions detected as a nodule. The method detected all the nodules without detecting blood vessels

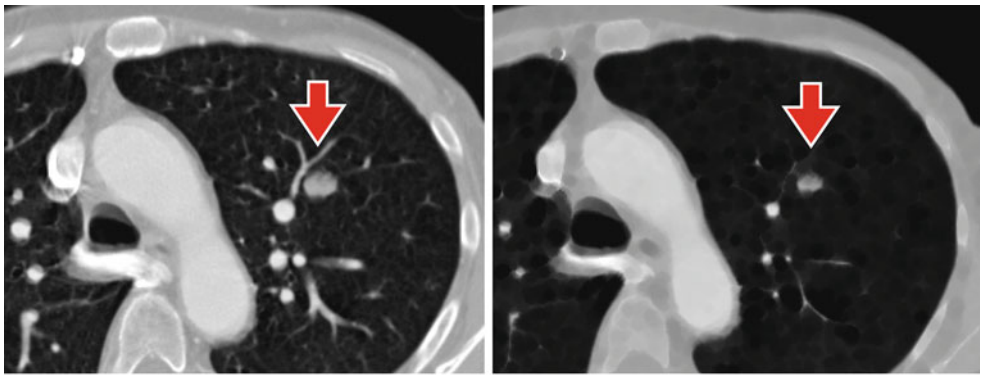

Fig. 5 Result of preprocessing. **a** Original image, and **b** image preprocessed by an erosion filter

blood vessels of diameters of 2, 3, 4, and 5 mm. The blood vessels were positioned at angles between 0 and 90° in relation to the X–Y slice image. Figure 4 shows the images of the digital phantom and detection result. The CNEF detected all the nodules without detecting blood vessels, as shown in Fig. 4c.

This result shows that the CNEF has the capability of nodule detection with regard to the detection of simple structure nodules and blood vessels.

Preprocessing for large CNEF

In this study, we employed two different filter sizes of CNEF. When large size of filter is used, sensitivity falls for nodules located close to the normal tissues such as blood vessels because filter overlaps with them. In order to separate the nodule from normal tissues, we introduced an erosion filter [22] as a preprocessing step, which shrinks the image of the blood vessels and nodules. Erosion filter is one kind of morphological filter, it enlarges the gap among objects.

Figure 5 shows original and preprocessed images. In Fig. 5b, the blood vessels have been shrunk; thus, the preprocessing filter improves the isolation of the nodule from the surrounding object. Furthermore, because the filter also shrinks the nodule, we can detect nodules using a filter with a smaller kernel. The use of a preprocessing filter thus reduces the number of calculations required.

Here, erosion filter may erase small nodules. To avoid it, this preprocessing is applied only when larger size of CNEF (filter diameter = 20 mm) is used. The diameter of erosion filter is set to 10 % of the filter diameter of CNEF.

False-positive reduction

Nodule candidates consist of true nodules and normal tissues such as blood vessels. There were typically about 5 FPs in a given slice image, and this number must be reduced to certain level for this technique to be effective. In this study, FPs (normal tissues) are distinguished from true positives (nodules) by analyzing the characteristic shape features followed by judgment using SVM. The procedure for FP reduction is performed as follows.

Step 1: Calculation of characteristic shape parameters
First, we outline the seven characteristic shape parameters. In every case except (iv) and (v), binary images are used (nodule candidate region: 1; background: 0).

(i) Area (X–Y, X–Z, and Y–Z planes)
Cross-sectional areas at the centre of the nodule candidate in the X–Y, X–Z, and Y–Z planes.

(ii) Surface area
The contour of the nodule candidate is determined in all slices belonging to the nodule candidate; the product of the total number of contour voxels and area of a single plane of the voxel is defined as the *surface area*.

(iii) Volume
The product of the total number of voxels inside the nodule candidate and volume of voxel is defined as the *volume*.

(iv) CT value
The CT value around the centre of the nodule candidate is calculated.

(v) Convergence
Basically, the CT value around the nodule is low; it increases from the surrounding area to the centre of nodule. In other words, gradient vectors of the voxel values around the nodule concentrate at the centre (Fig. 6a). For normal tissue, such as blood vessels, gradient vectors do not concentrate at the centre (Fig. 6b). Thus, we employ the

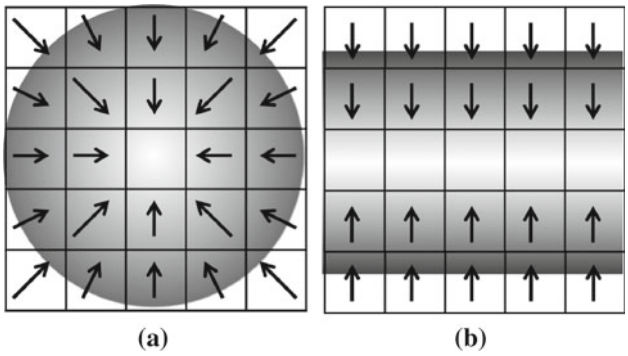

Fig. 6 Concentration of gradient vectors in a **a** nodule and **b** blood vessel

convergence in order to evaluate the concentration of voxel values [23].

To calculate this feature, the change in CT value of each point in the original image F in the x, y, and z directions was calculated as the gradient vector.

$$\vec{G} = (G_x, G_y, G_z) \tag{2}$$

$$G_x = \frac{\mathrm{d}F}{\mathrm{d}x}, G_y = \frac{\mathrm{d}F}{\mathrm{d}y}, G_z = \frac{\mathrm{d}F}{\mathrm{d}z} \tag{3}$$

Consequently, the inner product of the gradient vector in voxel value and the vector to the nodule centre at each voxel is calculated. The summation of such inner products is then defined as the *convergence*.

$$convergence = \sum_R \vec{G} \cdot \vec{C} \tag{4}$$

$\vec{C}$: Vector to the nodule center at each voxel.
R: Euclidean space

(vi) Diameter

When the diameters of the nodule and blood vessel are compared in the same volume, the former has a larger value. Thus, we introduced the diameter as a characteristic shape feature. The diameter is calculated in 3D; the minimum length of the segment that intersects the centre of a nodule candidate and has endpoints on the surface of the nodule candidate is defined as the *diameter*.

(vii) Overlapping area

Blood vessels exist throughout the lung region; however, nodules are usually isolated. To enhance this feature, a fixed sphere is placed at the centre of a nodule candidate; the ratio of the number of voxels that overlap the spherical surface and the nodule candidate to the number of voxels of the spherical surface is counted as the *overlapping area* (see Fig. 7). Regarding to the diameter of fixed sphere, we used 30 mm in the evaluation.

Step 2: Classification using SVM

To reduce the FP candidates using the seven characteristic shape features, we adopted the SVM algorithm [24,25], which is a type of learning machine based on statistical learning theory. SVM performs classification by constructing an N-dimensional hyperplane that optimally separates the data into two categories.

Practically, the input for the SVM is the seven characteristic values, and a judgment result is obtained from the output. Since SVM is a learning type classifier, it is trained using a large amount of data in advance. Here, the C-support vector classification (C-SVC) technique was used; the third polynomial function was used as the kernel function.

Experiments

In this section, the proposed method is evaluated to determine the effectiveness of the method. Firstly, the overall performance using the LIDC database is presented. The evaluation results for detection performance and calculation speed are then compared to existing methods.

Evaluation methods

In order to verify the performance of our proposed scheme, we performed an evaluation using chest CT images that were provided by the LIDC [26–28]. Since LIDC images were collected from several different institutions, spatial resolution and X-ray imaging parameters differed (slice intervals, 0.625–3.0 mm; in-plane resolution, 0.488–0.946 mm; tube voltage, 120–140 kV; and tube current, 40–499 mA).

In this study, we focused on nodules 5–20 mm in diameter, which at least one doctor among four pointed out as a nodule. We chose 84 cases from the LIDC database, which comprised a total of 103 nodules.

When the radiologists identified the nodule locations in each CT scan, they provided descriptors of the nodule characteristics such as likelihood of malignancy and subtlety. The number of radiologists that identify each nodule is valuable information for the evaluation of CAD. Thus, we introduced a characteristic called "agreement level" [17]. Nodules with an agreement level j represent nodules, which are marked by at least j of the 4 radiologists (where $j = 1, 2, 3, 4$).

Since detection performance may depend on the characteristics of malignancy, subtlety, and agreement level,

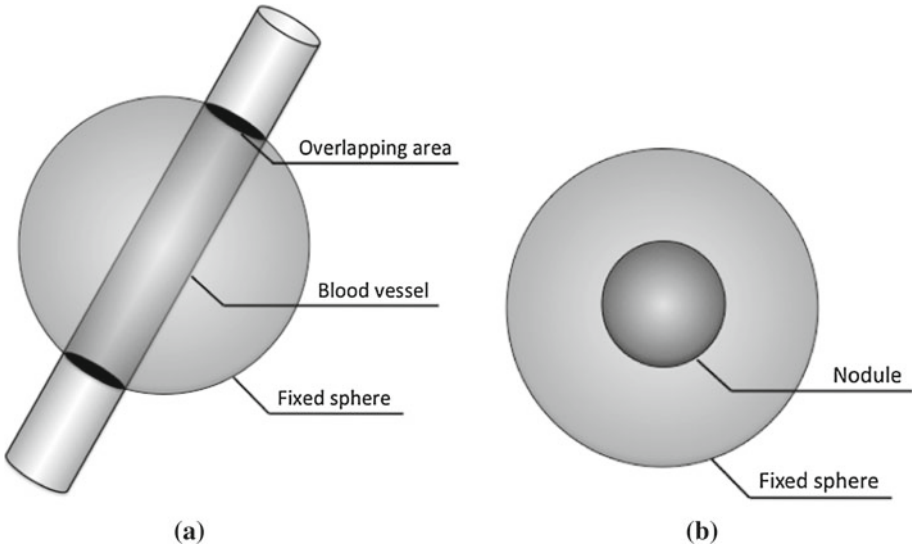

Fig. 7 Illustration for determining the overlapping area. **a** The blood vessel has a continuous structure and overlaps the fixed sphere. **b** When nodule is isolated and so no overlap occurs

Table 1 Number of nodules listed by agreement level, subtlety, and malignancy

	Category				
	1	2	3	4	5
Agreement level	103	84	64	33	–
Subtlety	4	15	25	34	25
Malignancy	2	22	57	16	6

we evaluated the detection performance by categorizing the nodules according to above three parameters. The numbers of nodules are listed in Table 1.

Regarding the detection parameters of the CNEF, we employed radii r_1 of 5–10 mm; a higher output was assumed to be the output value of each voxel. Erosion operation with a radius of 0.5 mm was applied for the former CNEF, and erosion with a radius of 1.0 mm was used for the latter one.

Nodule candidates obtained by the CNEF were classified into two classes using the SVM classifier aided by the characteristic shape features. In this experiment, we utilized the LIBSVM software library (version 2.71) [29]; C-SVC with the kernel of the 3rd polynomial function was introduced. These parameters were decided in a heuristic manner.

The nodule detection performance was evaluated by a so-called free-response receiver operating characteristic (FROC) curve. Slice images in each case were given, and sensitivity and FPs per case values were obtained. Here, sensitivity is defined as the ratio of the number of detected true nodules to the number of true nodules in the database and is expressed as a percentage. FP/case is defined as the ratio of the number of FPs to the number of cases employed for evaluation. Furthermore, the data of nodule candidates were randomly divided into five datasets; an evaluation by the cross-validation method was carried out.

Evaluation results

Figure 8 indicates the enhanced results by using CNEF. Filter output showed high value on the nodules, whereas most of the blood vessels had low values. Some small dots (indicated by black arrows) are shown in the enhanced images. They correspond to FPs being expected to be eliminated by FP reduction technique. Figure 9 shows the eliminated regions by using FP reduction technique. Most of the FPs were seen at the bifurcation of the blood vessels. These FPs were eliminated by SVM with characteristic features. Table 2 shows the characteristic features of nodules and FPs. In some results, characteristic features had significant difference between nodules and FPs. In other cases, SVM judged correctly using multiple features.

FROC curves of our proposed method are shown in Fig. 10.The solid line in the figure represents the FROC curve when FP reduction is disabled. The dashed line represents the curve when FP reduction is employed. Using the FP reduction method, FPs were reduced to about 20 %. The proposed method is able to detect 80 % of all nodules in the data set with 4.2 FPs per case.

Figure 11 presents multiple FROC curves classified according to subtlety ratings. Subtlety ratings were merged into three classes. Obvious nodules (subtlety = 4 and 5) are detected at a sensitivity of 90 % with 4.2 FPs per case. On the other hand, the sensitivity of subtle nodules (subtlety = 1 and 2) is less than 50 %.

FROC curves classified according to the likelihood of malignancy are shown in Fig. 12. The sensitivity reached 95 % for nodules with a high malignancy rate (malignancy = 4 and 5). For nodules with a low malignancy rate (malignancy = 1 and 2), sensitivities were about 20 % lower than those of the high malignancy rate.

Figure 13 shows multiple FROC curves according to agreement level. Overall, the sensitivity of nodules with an

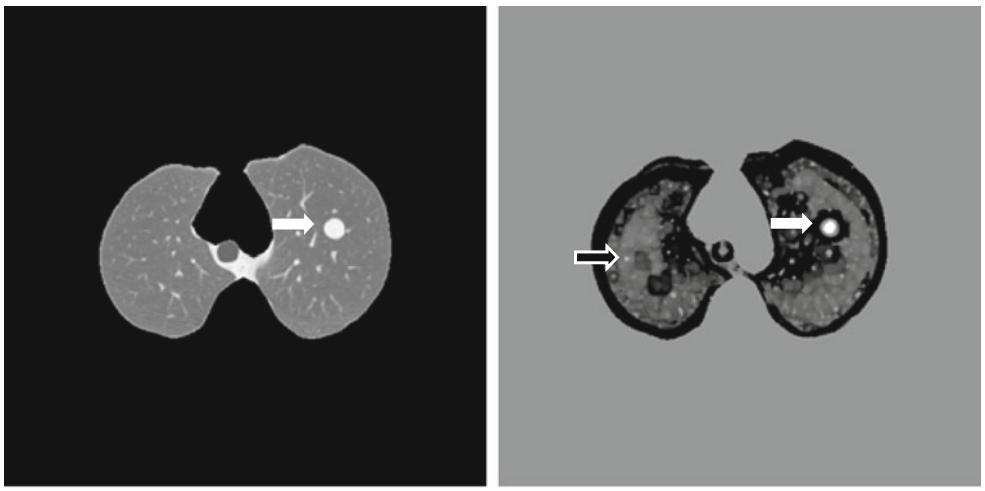

(a)

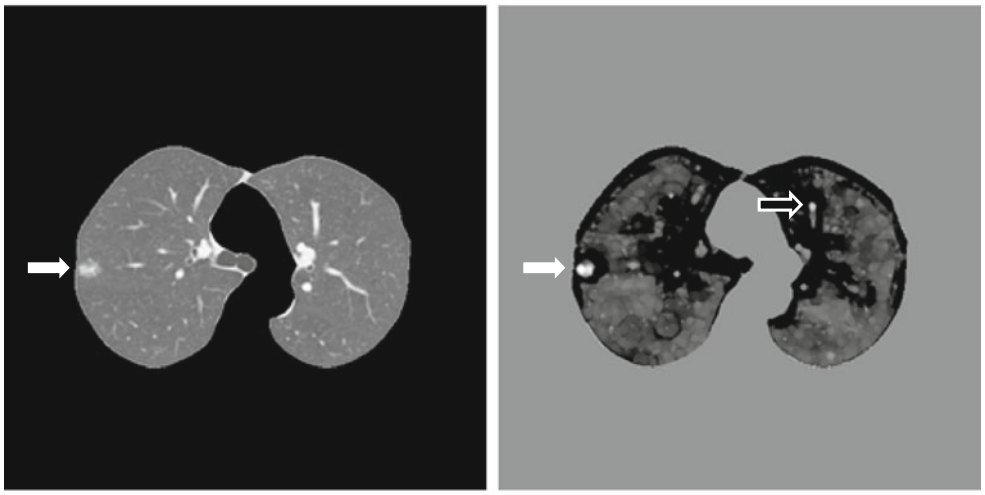

(b)

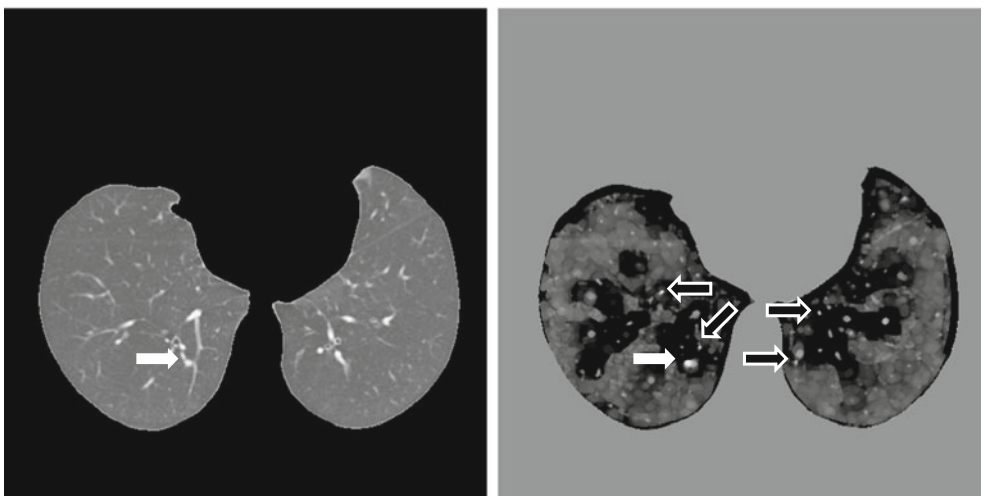

(c)

Fig. 8 Nodule enhanced results using proposed CNEF. *Left* and *right* images are original and nodule-enhanced images, respectively. *White* and *black arrows* indicate the nodules and FPs, respectively

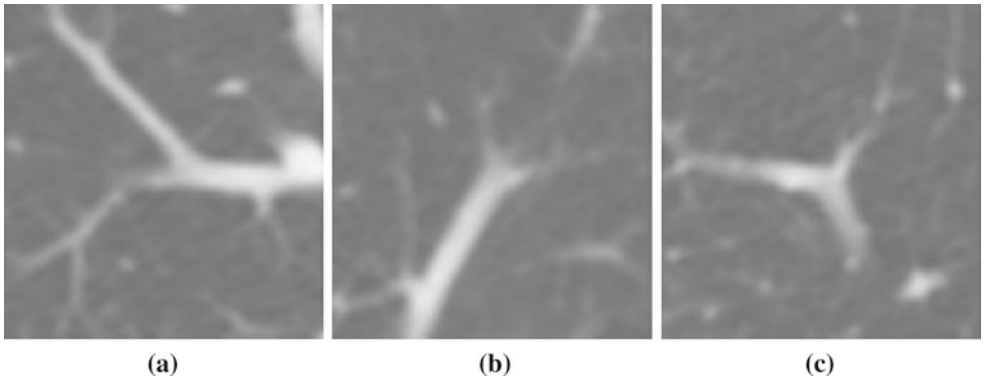

Fig. 9 Eliminated regions by using FP reduction method. Eliminated regions are located in the centre of these images

Table 2 Examples of characteristic features of nodules (Fig. 8) and FPs (Fig. 9)

	Area (mm^2)			Volume (mm^3)	Surface area (mm^2)	CT value (H.U.)	Convergence	Diameter (mm)	Overlapping area (%)
	X–Y	*X–Z*	*Y–Z*						
Nodule Fig. 8a	208.6	241.0	214.3	2432.4	1249.8	78	1.00	13.3	0.8
Nodule Fig. 8b	114.6	74.5	63.5	1509.7	1818.3	101	0.98	3.0	24.7
Nodule Fig. 8c	159.2	194.0	131.8	2064.2	2233.1	−41	0.99	5.5	14.4
FP Fig. 9a	151.1	157.9	70.6	1977.7	2081.5	−61	0.90	4.1	29.7
FP Fig. 9b	103.0	39.2	55.4	1112.3	1287.5	−171	0.88	3.2	14.4
FP Fig. 9c	85.7	87.8	55.9	961.1	1075.8	11	0.90	4.3	7.4

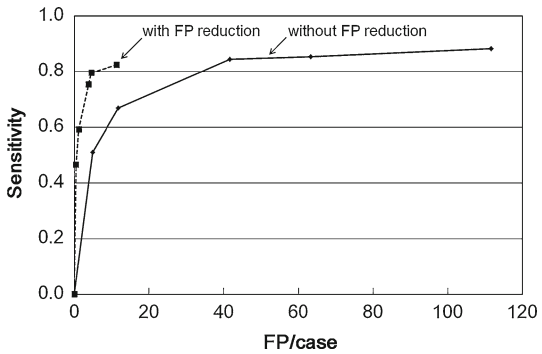

Fig. 10 FROC curves of the proposed method

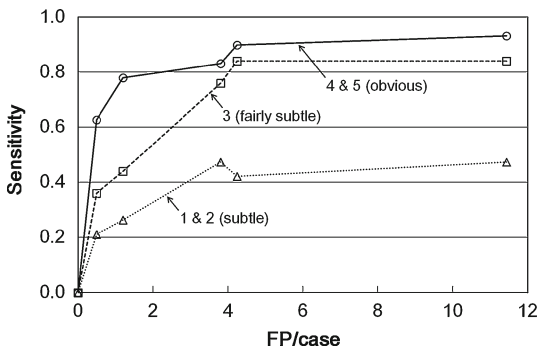

Fig. 11 FROC curves classified according to subtlety ratings. Obvious nodules are detected at a sensitivity of 90 % with 4.2 FPs per case. On the other hand, the sensitivity of subtle nodules is less than 50 %

agreement level of 4 was 10 % better than that with the level of 1.

Most obvious and malignant nodules were solid nodules with high contrast and a clear outline. The majority of nodules with low subtlety or malignancy were classified into a ground glass opacity (GGO) nodule that has low contrast. The above results indicate that the proposed method has the highest sensitivity for a nodule with a clear outline and high contrast. On the other hand, there is a need to improve the sensitivity for GGO nodules.

As for the effectiveness of preprocessing (erosion filter), we compared with and without preprocessing. Under the same FP rate (4.0/case), sensitivity of without preprocessing was 59.2 %, whereas with preprocessing was 80.0 %. The nodule shown in Fig. 5 is one undetected solely by the filter, but detected with preprocessing. These results indicate that preprocessing works well in our CAD scheme.

Figure 14 shows examples of the detection results for nodules that were detected correctly with 4.2 FPs per case and a sensitivity of 80 %. Isolated nodules were detected correctly, while blood vessels that had a continuous shape were correctly not detected. On the other hand, Fig. 15 shows nodules that remained undetected. The main reasons for misdetection were (1) insufficient contrast of the nodule and (2) nodules adhered to the thoracic wall or blood vessel. Among the nodules that adhered to the thoracic wall, nodules were detected

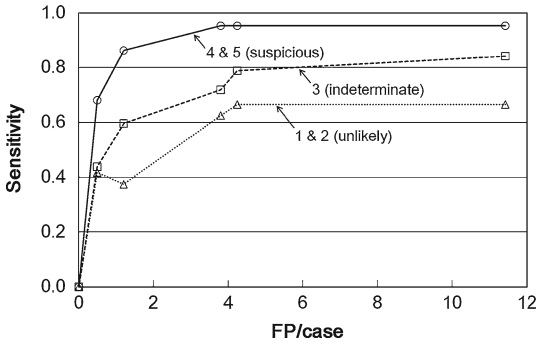

Fig. 12 FROC curves classified according to likelihood of malignancy. A high detection rate was obtained for nodules with high malignancy rates

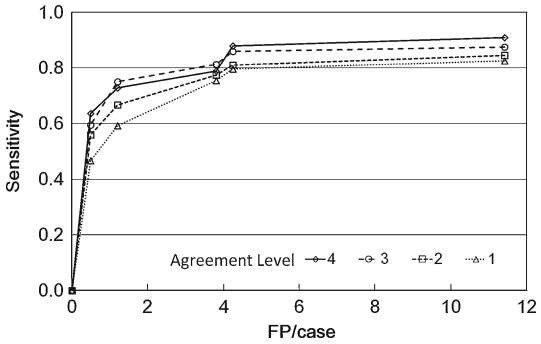

Fig. 13 FROC curves classified according to agreement level. The sensitivity of nodules with an agreement level of 4 was 10 % better than that with an agreement level of 1. 87 % of nodules with an agreement level of 4 are detected at 4.2 FPs per case

correctly when they were incorporated into lung region at the lung segmentation process. However, nodules outside lung region were missed. We plan to improve the detection capability for such cases by including other detection methods.

Comparison with existing methods

We also compared the detection capability and speed with those of existing methods. We selected 7 CAD schemes that show detection capability using the LIDC database or reported detection speed. Although it is difficult to compare because detection performance depends on image datasets (e.g., number of cases, target nodule size, scanning protocol) and detection parameters, it is still important to attempt making relative comparison. The summary of comparison is shown in Table 3.The performance of our method is similar to or better than the existing methods. As mentioned in Section *Experiments*, LIDC images were collected from several different institutions, and the quality of the CT images differed among institutions. Therefore, the evaluation of the detection performance using LIDC was much more challenging than evaluation performed for images acquired from a single institution. Sensitivity and FP/case in our method were preferable despite the challenges.

The detection speed for our method, including FP reduction, is 25–34 s per case using a 2.8 GHz personal computer. This is 4–36 times faster than existing methods. The detection speed of our method is equivalent to or faster than the image acquisition time of a CT unit.

With regard to filter shape, some CAD schemes introduced a spherical filter [3,30]. Spherical filters enable isotropic processing. However, they require many calculations. In our method, the spherical filter was replaced with a cylindrical shape filter in order to reduce the number of calculations. Experimental results showed that the detection performance was the same as with conventional methods. Since the current scan parameter of slice pitch for lung cancer screening is wider (5–10 mm), image information is poorer in the z direction than in the x and y directions. Therefore, CNEF is a convenient nodule-enhancement filter for cancer screening conditions from the point of view of both detection performance and calculation time.

Conclusions

In this study, we have proposed a novel filter to increase the calculation speed of 3D nodule detection in chest CT images. The proposed method introduces a cylindrical shape filter as a nodule enhancement. This filter shape remarkably reduces the number of calculations. Furthermore, we introduced a FP reduction method using seven characteristic shape features and SVM.

In the experiments, the overall performance using the LIDC database was evaluated. We demonstrated that proposed method was able to detect 80 % of all nodules in the data set with 4.2 FPs per case. This result shows that, compared with existing methods, our method performs at a similar or better level. As for the detection speed, our method is 4–36 times faster than existing methods and equivalent to or faster than the image acquisition speed of a CT unit.

Reducing the gap between image acquisition time and nodule detection time means that we will have the capability to perform additional examinations, such as high-resolution scanning, while keeping the patient on the bed of the CT unit. Therefore, our proposed method may be useful in clinical practice for nodule detection in chest CT images.

Our future research will focus on improving the detection rate. Most undetected nodules were GGO or part-solid nodules that were attached to or close to the lung wall or blood vessels. We plan to improve the detection capability for such cases by including other detection methods.

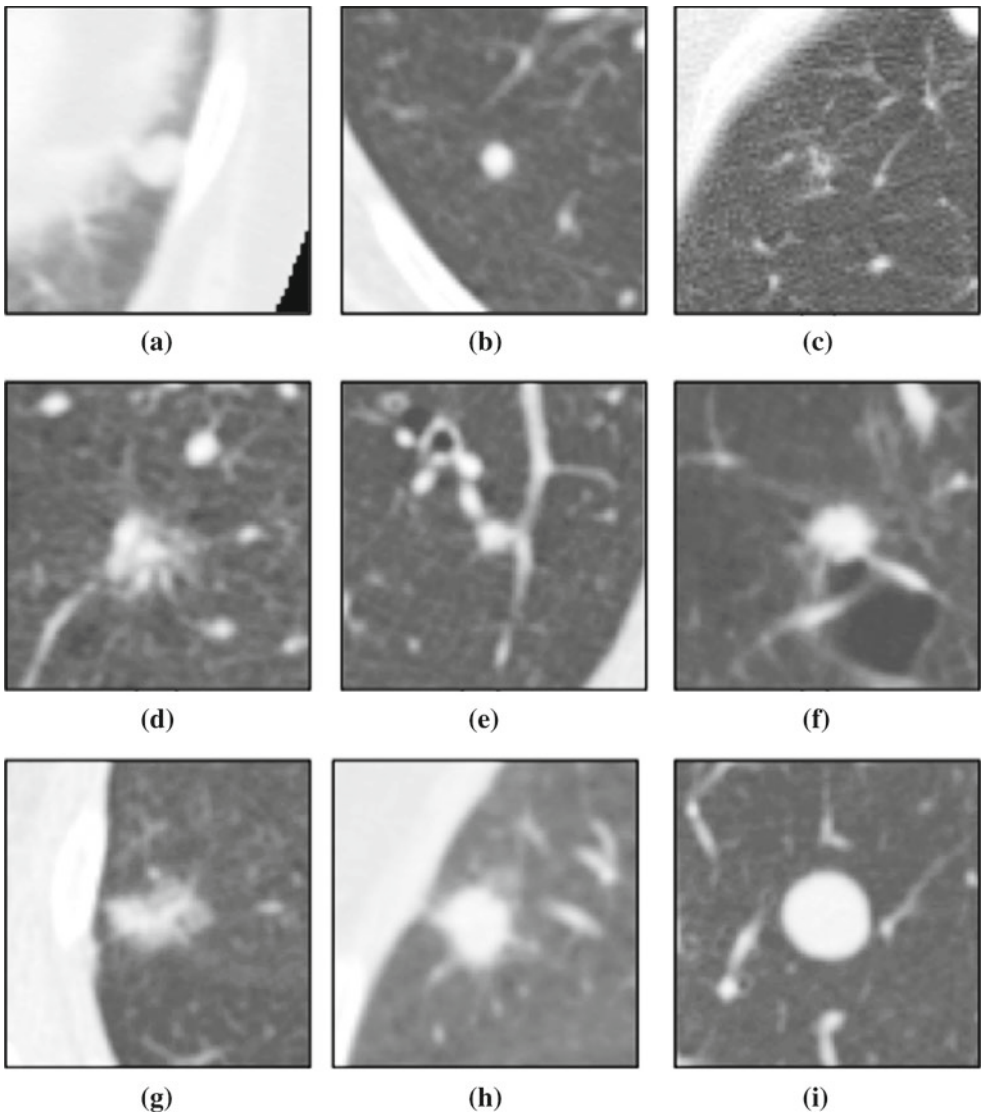

Fig. 14 Nodule images detected by the CAD scheme with 4.2 FPs per case and a sensitivity of 80 %. The nodules detected by the proposed method are located in the centre of the images

Table 3 Performance comparison of proposed method with existing methods

CAD system	Image database	Number of cases	Number of nodules	Agreement level	Sensitivity (%)	FPs/case	Detection time (seconds)
Way et al. and Sahiner et al. [13,14]	LIDC	48	73	1	79.0	4.9	–
Opfer and Wiemker [15]	LIDC	–	127	1	76.0	4.0	180–300
Golosio et al. [16]	LIDC	84	148	1	45.0	4.0	–
Messey et al. [17]	LIDC	84	143	1	82.5	4.0	135–165
Riccardi et al. [18]	LIDC	154	387	1	49.0	4.0	–
Chamarlinghi et al. [19]	LIDC	138	252	2	80.0	4.0	–
Tan et al. [20]	LIDC	125	259	1	66.4	3.0	–
Proposed method	LIDC	84	103	1	80.0	4.2	25–34

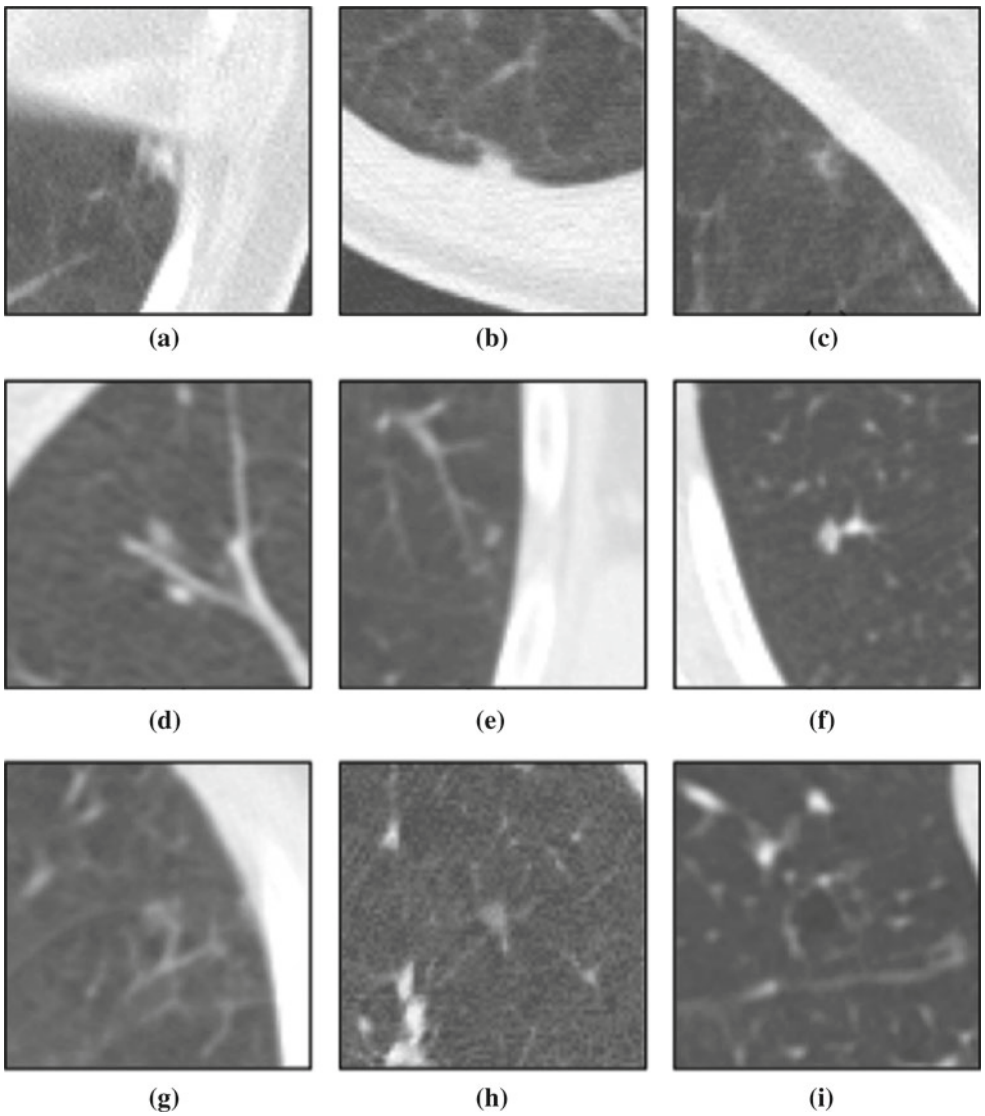

Fig. 15 Nodules that remained undetected in the CAD scheme. The nodule is located in the centre of the image. **a–c** Nodules touching or close to the lung wall. **d–f** Nodules touching or close to the blood vessels. **g–i** Nodules with low contrast

Recently, some hospitals have begun to apply PET/CT examinations to cancer screening. We plan to introduce this method to the CAD scheme for PET/CT images.

Conflict of interest None.

References

1. Sone S, Takashima S, Li F, Yang Z, Honda T, Maruyama Y et al (1998) Mass screening for lung cancer with mobile spiral computed tomography scanner. Lancet 351:1242–1245
2. National Lung Screening Trial. Information is available at http://www.cancer.gov/clinicaltrials/noteworthy-trials/nlst
3. Yamamoto S, Matsumoto M, Tateno Y, Iinuma T, Matsumoto T (1996) filter—a new filter based on mathematical morphology to extract the isolated shadow, and its application to automatic detection of lung cancer in X-ray CT. Proc 13th Int Conf Pattern Recognit 2:3–7
4. Lee Y, Hara T, Fujita H, Itoh S, Ishigaki T (2001) Automated detection of pulmonary nodules in helical CT images based on an improved template-matching technique. IEEE Trans Med Imaging 20(7):595–604
5. Shah SK, McNitt-Gray MF, Rogers SR, Goldin JG, Suh RD, Sayre JW et al (2005) Computer aided characterization of the solitary pulmonary nodule using volumetric and contrast enhancement features. Acad Radiol 12(10):1310–1319
6. Li W (2007) Recent progress in computer-aided diagnosis of lung nodules on thin-section CT. Comput Med Imaging Graph 31 (4–5):248–257
7. Li Q, Li F, Doi K (2008) Computerized detection of lung nodules in thin-section CT images by use of selective enhancement filters and an automated rule-based classifier. Acad Radiol 15(2):165–175
8. Pu J, Zheng B, Leader JK et al (2008) An automated CT based lung nodule detection scheme using geometric analysis of signed distance field. Med Phys 35(8):3453–3461
9. Matsumoto S, Ohno Y, Yamagata H et al (2008) Computer-aided detection of lung nodules on multidetector row computed tomog-

raphy using three-dimensional analysis of nodule candidates and their surroundings. Radiat Med 26(9):9–562
10. Suzuki K (2009) Asupervised 'lesion-enhancement' filter by use of a massive-training artificial neural network (MTANN) in computer-aided diagnosis (CAD). Phys Med Biol 54(18):S31–45
11. Murphy K, van Ginneken B, Schilham AM et al (2009) A large-scale evaluation of automatic pulmonary nodule detection in chest CT using local image features and k-nearest-neighbour classification. Med Image Anal 13(5):757–770
12. Sousa JR, Silva AC, de Paiva AC et al (2010) Methodology for automatic detection of lung nodules in computerized tomography images. Comput Methods Programs Biomed 98(1):1–14
13. Way TW, Hadjiiski LM, Sahiner B, Chan HP, Cascade PN, Kazerooni EA et al (2006) Computer-aided diagnosis of pulmonary nodules on CT scans: segmentation and classification using 3D active contours. Med Phys 33:2323–2337
14. Sahiner B, Hadjiiski LM, Chan HP, Shi J, Cascade PN, Kazerooni EA et al (2007) Effect of CAD on radiologists' detection of lung nodules on thoracic CT scans: observer performance study. Proc SPIE Med Imaging 6515(65151D):1–7
15. Opfer R, Wiemker R (2007) Performance analysis for computer-aided lung nodule detection on LIDC data. Proc SPIE Med Imaging 6515(65151C):1–9
16. Golosio B, Masala GL, Piccioli A, Oliva P, Carpinelli M (2009) A novel multithreshold method for nodule detection in lung CT. Med Phys 36(8):3607–3618
17. Messay T, Hardie R, Rogers S (2010) A new computationally efficient CAD system for pulmonary nodule detection in CT imagery. Med Image Anal 14(3):390–406
18. Riccardi A, Petkov TS, Ferri G, Masotti M, Campanini R (2011) Computer-aided detection of lung nodules via 3D fast radial transform, scale space representation, and Zernike MIP classification. Med Phys 38(4):1962–1971
19. Camarlinghi N, Gori I, Retico A, Bellotti R et al (2011) Combination of computer-aided detection algorithms for automatic lung nodule identification. Int J CARS 7(3):455–464
20. Tan M, Deklerck R, Jansen B et al (2011) A novel computer-aided lung nodule detection system for CT images. Med Phys 38(10):5630–5645
21. Hardie RC, Rogers SK, Wilson T, Rogers A (2008) Performance analysis of a new computer aided detection system for identifying lung nodules on chest radiographs. Med Image Anal 12(3):240–258
22. Charles RG, Edward RD (1988) Morphological methods in image and signal processing. Prentice Hall, New Jersey
23. Kobatake H, Hashimoto S (1999) Convergence index filter for vector fields. IEEETrans Image Proc 8(8):1029–1038
24. Cristianini N, Shawe-Taylor J (2000) An introduction to support vector machines and other kernel-based learning methods. Cambridge University Press, Cambridge
25. Burges CJC (1998) Tutorial on support vector machines for pattern recognition. Data Min Knowl Disc 2(2):121–167
26. LIDC lung nodule image database. National cancer imaging archive at https://imaging.nci.nih.gov/ncia/
27. Armato SG III, Roberts RY, McNitt-Gray MF, Meyer CR, Reeves AP, McLennan G et al (2007) The lung image database consortium (LIDC): ensuring the integrity of expert-defined. Acad Radiol 14:1455–1463
28. McNitt-Gray MF, Armato SG III, Meyer CR, Reeves AP, McLennan G, Pais RC et al (2007) The lung image database consortium (LIDC) data collection process for nodule detection and annotation. Acad Radiol 14:1464–1474
29. Chang CC, Lin CJ. LIBSVM: a library for support vector machines. Software available at http://www.csie.ntu.edu.tw/cjlin/libsvm/
30. Dehmeshki J, Ye X, Lin X, Valdivieso M, Amin H (2007) Automated detection of lung nodules in CT images using shape-based generic algorithm. Comput Med Imaging Graph 31(6):408–417